# Multivariate Approach for Studying the Degradation of Perovskite Solar Cells.

Kettle, Jeffrey; Tyagi, Priyanka; David, Tudur; Stoichkov, Vasil

## Solar Energy

1  **Multivariate Approach for Studying the Degradation of Perovskite Solar Cells**

2  **Priyanka Tyagi, Tudur W. David, Vasil D. Stoichkov, Jeff Kettle***

3  School of Electronic Engineering, Bangor University, Dean St., Bangor, Gwynedd, Wales, UK,

4  *email; j.kettle@bangor.ac.uk

5

## Abstract

7  Despite the progress in the performance of perovskite solar cells (PSCs), the absorber layer
8  degradation during prolonged exposure to multiple environmental conditions is still a major
9  issue. As the degradation depends upon many intrinsic and extrinsic factors, the need to adopt a
10  multivariate testing protocol, which provides rapid assessment of device stability, is required. To
11  do this, a Plackett Burman (PB) screening design has been used to analyze 9 different factors that
12  affect the PSC stability; including four extrinsic factors (oxygen, moisture, UV exposure and
13  temperature) and five intrinsic factors (selection of hole transport layer and electron transport
14  layer, absorber layer thickness, halide type and perovskite deposition process). This approach
15  allows us to rank the relative severity of these factors and can be used to narrow the scope of
16  materials and device architectures to be modified, by identifying materials and configurations,
17  which are the most stable. The least and most stable device configurations have been identified
18  and the success of the screening approach has been demonstrated by testing the optimized
19  configurations under ISOS-D1 and –L2 protocols. Importantly, only 12 experiments are needed
20  to establish the most stable combination from the 9 factors thus providing a rapid assessment.
21  Scanning electron microscopy (SEM) and X-ray diffraction (XRD) measurements of perovskite
22  absorber films have been performed in order to understand the degradation pathways and to
23  support the conclusion of PB screening technique.

24  **Key words;** perovskite solar cells, stability, multivariate analysis, degradation studies.

25

26

## Introduction

Perovskite solar cells (PSCs) have attracted attention due to the rapid growth in power conversion efficiencies (PCEs) over the past decade (Saliba et al., 2016; Li at al., 2016) and the possibility to integrate them in tandem configuration with traditional silicon solar cells (Sahli et al., 2018; Kanda et al., 2018). However, the poor stability remains a challenge for their commercialization. The sources of instability in PSCs are numerous and include intrinsic properties (perovskite layer composition, hole and electron transporter, electrode etc.) (Boyd et al., 2019; Christians et al., 2018a; Cao et al., 2018) and external environmental conditions such as humidity, light, temperature and thermal changes etc. Most studies on PSC stability to date have been focused on considering one or a maximum of two stress factors e.g. oxygen ($O_2$) (Bryant et al., 2016; Kong et al., 2016) humidity (Song et al., 2016a; Schlipf et al., 2019) or temperature (Misra et al., 2015). Although the stability study under one applied stress can provide meaningful information, it does not provide information about the likely outdoor stability during which multiple stresses are simultaneously applied. This is important for three reasons; firstly, the outdoor environment is the most likely location for deployment, so PSCs will experience multiple stresses, which will act simultaneously and vary with time (Christians et al., 2018b) Secondly, it has been observed that the degradation is accelerated due to the 'interaction' between stress factors. Thirdly, and surprisingly, it has been shown in PSCs that one stress factor can also act as the trigger to the degradation from other stresses; an example being that methyl ammonium lead iodide (MAPbI$_3$) absorber layer does not degrade rapidly due to illumination unless the samples are heated at above 45ºC (Misra et al., 2015).

Some recent advancement has happened in the degradation studies of PSCs under the combined stress factors (2 or 3 at a time). Christians et al. have studied the degradation of triple cation based PSCs (> 1000h) under the effect of three stress factors; light (including UV-light, $O_2$ and moisture) (Christians et al., 2018a). Domanski et al have made a very significant contribution in their study, where they have presented the impact of $O_2$, humidity, and temperature on the operational stability of PSCs. The authors have presented a degradation study of PSCs under one stress and in the combination of multi-stress factors. They have observed that the PSCs degrade drastically in the presence of $O_2$ and humidity (even 5%) and were very unstable at elevated

56  temperature (~ $65^0$C). Based on their observations, they have also proposed the stable
57  operational conditions for the PSCs (Domanski et al., 2018).

58  Another very important study on the degradation of MAPbI$_3$ absorber layer based PSCs has been
59  performed by Islam and coworkers where they have performed maximum power point tracking
60  (MPPT) under continuous light illumination for 4000 h. This study is very important as this is
61  possibly the longest MPPT till date performed on MAPbI$_3$ based PSCs without mixing of cations
62  in the formulation of perovskite. The studies were performed on encapsulated devices at $30^0$C
63  without UV filters (Islam et al., 2019).

64      Given the numerous and unknown range of variables that affect PSC stability, a holistic
65  approach to study stability in PSCs would be beneficial to the community. This would enable
66  multiple extrinsic and intrinsic factors to be modified simultaneously and their stability assessed
67  together rather than by 'one factor at a time'. However, such a 'multi-stress' study in conjunction
68  with device structure variation would be very time-consuming undertaking, particularly if only
69  one factor was changed for every experiment. Therefore, we propose to use an experimental
70  screening design from design of experiments (DOE) method, which allows us to undertake
71  multivariate analysis of the PSC stability. Multivariate analysis techniques such as plackett
72  burman (PB) have been widely used by the manufacturing and life science industry for process
73  optimization, demonstrating the validity of this mathematical approach (Waśko et al., 2010;
74  Alves et al., 2014, Briefs at al., 2013; Jain et al., 2010). Recently, our group has successfully
75  demonstrated the applicability of PB screening in the performance optimization of field effect
76  transistors (FETs) with 8 factors in 12 experimental runs (Gomes et al., 2019).

77      It can also be used in the context of PSC reliability by identifying the principle factors
78  that impact upon stability and aid the design of the PSC to be more stable to extrinsic stress
79  factors. The approach allows us to 1) rank which intrinsic or extrinsic degradation factor affects
80  the stability the most and the least and 2) Identify which combination of device
81  structure/materials yields the most stable device. To complement the statistical analysis, X-Ray
82  diffraction (XRD) and scanning electron microscopy (SEM) measurements were performed to
83  understand fully the degradation routes for each stress and change in device structure.

In this work, multiple factors were studied by using the PB screening technique, which can identify the most significant degradation factors using a low number of test runs. The screening technique is capable of testing factors by requiring only $n+1$ experiments (Waśko et al., 2010; Alves et al., 2014; Briefs at al., 2013; Jain et al., 2010). This means a rapid analysis can be achieved. PB analysis utilizes a predetermined test matrix based upon the number of factors selected and the matrix used for this test was taken from Esbensen et al (Esbensen et al., 2018). Four extrinsic stress factors ($O_2$, humidity, UV exposure and temperature) and five intrinsic factors related to device structure (HTL and ETL, absorber layer thickness, absorber layer composition (MAPbI$_3$ or MAPbBr$_2$I) and fabrication procedure) were studied for an 'inverted' PSC structure. The PSC device structure is shown in Fig.1. For the study, two levels for each factor were considered. Based upon the number of factors selected, 12 experiments were found to be necessary, based upon the PB table.

## 2.  Experimental details

### 2.1. Design of experiments and choice of levels/factors

Table 1 and 2 show the detailed range of stress conditions used in each experiment, where 'L' indicates the low level and 'H' indicates the high level, which can be quantitative or qualitative. The 'L' and the 'H' levels, corresponding to each factor, were chosen based upon their impact on the stability of the PSCs sited in the previous literature. We have selected poly(3,4-ethylenedioxythiophene)-poly(styrenesulfonate)(PEDOT:PSS) as 'L' level for the factor HTL as it is widely used HTL in inverted PSCs (Xiao et al., 2014; You et al., 2014)  and is found very unstable compared to inorganic HTL due to the hygroscopic nature of this layer (You et al., 2016). In contrast to PEDOT:PSS, nickel oxide (NiO$_x$) is reported as a very stable HTL in inverted PSCs (You et al., 2016;  Kim et al., 2015; Zhou et al. 2018) which justified the choice of this material as the 'H' level for HTL. For Perovskite absorber layer, MAPbI$_3$ and MAPbBr$_2$I have been chosen as the 'L' and 'H' levels respectively. MAPbI$_3$ is very well studied and widely used absorber layer due to their near complete visible light absorption in the films and efficient charge extraction due to a high diffusion length for the carriers (Strabks et al., 2013; Lopez et al., 2017). This absorber layer showed high sensitivity and instability towards moisture and $O_2$ (Bryant et al., 2016). MAPbBr$_3$ shows better resistance towards moisture and $O_2$ due to its

crystallographic structure but at a cost of large exciton binding energy and reduced light absorption, resulting in low PCE in PSCs (Lopez et al., 2017; Edri et al.; 2013). Therefore, we have selected MAPbBr$_2$I as 'H' level to compensate for the efficiency and stability (Zhao et al., 2014). For ETL, with and without lithium fluoride (LiF)/ [6,6]-Phenyl-C71-butyric acid methyl ester (PC$_{70}$BM) interface were chosen as the 'H' and 'L' levels because the presence of electron injection layer improves the stability and reduces hysteresis in PSCs (Wang et al., 2017). LiF was chosen because it is found to improve the efficiency of the PSCs by the doping of PCBM (Turak et al., 2017). For the fabrication steps, two-step procedure was considered as 'H' level because it provides a better reproducibility as compare to the one-step procedure ('L' level) (Li et al., 2016; Xiao et al., 2014). Thick films were considered as the 'L' level because the devices consisting thick films were found least efficient due to the increase in recombination resistance of the absorber layer as compared to the devices with thin absorber layer (~300nm) ('H' level) (Liu et al., 2014).

The selection of the extrinsic factors is quantitative. UV exposure degrades the devices faster, especially in the presence of O$_2$ (Christians et al., 2018a) so 'with UV filter' and 'without UV filter' have been taken as 'L' and 'H' levels. The 'L' (0%) and 'H' (20%) levels for O$_2$ correspond to the measurements performed in Nitrogen (N$_2$) and air. For humidity 'L' (< 5%) and 'H' (80%) corresponds to the inert-dry conditions and ambient humidity. The 'H' level of temperature is related to previous literature and the 'ISOS' standards which controls temperature at 65$^o$C during accelerated testing. The 'L' level was kept as 45$^o$C, as this is the lower temperature limit for a solar cell under 1 sun illumination (Koehl et al., 2011; Misra et al., 2015).

It is worth noting that the choice of these levels could be different for other set of experiments, which could lead different resulting conclusions. For the 2-fold PB screening technique, we are restricted to a choice of only two levels related to each factor. These levels are summarized in the table below.

143    **Table 1**: Plackett-Burman (PB) table used which requires 12 experiments to study the main

144    effects of degradation to the perovskite absorber layer.

| | Extrinsic Factors | | | | Intrinsic Factors | | | | |
|------|------|----------|------|------|--------|------|------|---------------------|-----------|
| Run | $O_2$ | Humidity | UV | T | Halide | HTL | ETL | Fabrication Step | Thickness |
| 1. | L | L | L | L | L | H | L | H | L |
| 2. | H | H | H | L | H | H | L | H | L |
| 3. | H | H | L | L | H | L | H | L | L |
| 4. | H | L | H | L | L | L | H | H | H |
| 5. | L | H | H | L | L | H | H | L | H |
| 6. | L | L | H | L | H | L | L | L | H |
| 7. | H | L | L | H | L | L | L | L | L |
| 8. | L | H | L | H | H | L | L | H | H |
| 9. | H | L | L | H | H | H | H | H | H |
| 10. | L | H | H | H | L | L | H | H | L |
| 11. | H | H | H | H | L | H | L | L | H |
| 12. | L | L | H | H | H | H | H | L | L |

145

146    **Table 2**: Definition of each low ('L') and high ('H') factor defined in table 1.

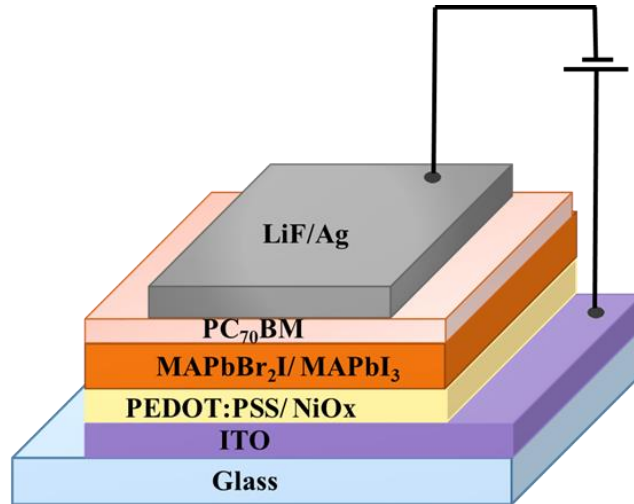| | $O_2$ | Humidity | UV | T | Halide | HTL | ETL | Fabrication Step | Thickness |
|---|-----|----------|-----------------|-----------|-----------|-----------|-------------|------------------|-----------|
| L | 0% | $< 5\%$ | With UV filter | $45^{\circ}C$ | $MAPbI_3$ | PEDOT:PSS | Without LiF | one-step | 500nm |
| H | 20% | 80% | Without UV filter | $65^{0}C$ | $MAPbBr_2I$ | NiOx | With LiF | two-step | 280nm |

147

148

149

150

151

152

153



154    **Fig. 1: Schematic of Device configuration used for stability studies.**

155 A 'run' in table 1 is defined as the individual experiment where the device configuration and
156 stress factors are altered. For clarity, a table has been added to the *SI (Table S1)* explicitly stating
157 the configuration and conditions used in 12 experimental runs.

## 2.2. Perovskite absorber layers and Device Fabrication

159 Samples for each run were fabricated on glass substrates, which were cleaned by ultra sonicating
160 in deionized water, acetone and isopropanol for 20 min each, followed by $O_2$ plasma treatment
161 for 5 min. The variation in sample configuration was considered by using two HTLs;
162 PEDOT:PSS and $NiO_x$, two compositions of perovskite ($MAPbI_3$, $MAPbBr_2I$; each with two
163 thicknesses), perovskite layer deposition by either one-step or two-step process and including or
164 excluding the ETL (LiF).

165 Shown in table 2 are the 'L' and 'H' levels used for this study. PEDOT:PSS (Ossila
166 Al4083) was spin coated at 4000 rpm for 40 s in ambient conditions and annealed at $150^{\circ}$C for
167 15 min. $NiO_x$ solution was prepared by dissolving nickel nitrate hexahydrate ($Ni(NO_3)_2.6H_2O$)
168 and ethylenediamine in 1:1 molar ratio in ethylene glycol (all from Sigma Aldrich). The solution
169 was then left for stirring at $70^{\circ}$C for 3 h. $NiO_x$ films were deposited at 2000rpm for 90 s followed
170 by annealing at $300^{\circ}$C for 1 h in ambient conditions.

171 For the perovskite layer, three factors were varied; (i) the perovskite composition -
172 $MAPbI_3$ or $MAPbBr_2I$, (ii) perovskite absorber layer thickness and (iii) the deposition process
173 (one-step or two-step). The perovskite absorber layers were deposited in a $N_2$ filled glove box.
174 For one-step Process, The $MAPbI_3$ solution was prepared by mixing lead iodide ($PbI_2$) and
175 methylammonium iodide (MAI) in 1:1 M ratio in dimethylformamide (DMF). The solution was
176 left on stirring for 24 h at room temperature and heated at $70^{\circ}$C for 10 min and during the
177 deposition. The solution was filtered by using a 0.45 µm PTFE filter. The films were deposited at
178 2000 rpm and 6000 rpm for 40 sec with an anti-solvent (toluene) treatment in last 10 sec of spin
179 coating. Samples were annealed at $90^{\circ}$C for 1 h after the deposition. The measured thicknesses of
180 perovskite layer were approximately 500 nm and 280 nm for 2000 rpm and 6000 rpm films.
181 $MAPbBr_2I$ solution was prepared by mixing 433 mg lead bromide ($PbBr_2$) and 187.6 mg MAI in
182 1 ml DMF. The remainder of the solution preparation and film fabrication was kept the same as
183 for $MAPbI_3$. To deposit $MAPbI_3$ by two-step process, separate solutions of MAI (30 mg/ml) in
184 isopropanol and $PbI_2$ (461 mg/ml) in DMF were prepared. $PbI_2$ solution was spin coated at 2000

185   rpm and 6000 rpm for 40 sec on substrates from a solution heated at $70^0C$ for 10 min. Substrates

186   were then annealed at $90^oC$ for 20 min. Subsequently, MAI was deposited at 6000 rpm for 40 sec

187   and films were annealed at $90^oC$ for 20 min. Similarly, for $MAPbBr_2I$, the concentration of

188   solution was 30 mg/ml in isopropanol for MAI and 367 mg/ml in DMF for $PbBr_2$. The spin

189   coating procedure was similar to that of the $MAPbI_3$. Both the $PbI_2$ and $PbBr_2$ solutions were

190   filtered using a 0.45 µm PTFE filter.

191        After perovskite layer deposition $PC_{70}BM$ was deposited at 4000 rpm for 40 sec from a

192   solution of 30 mg/ml $PC_{70}BM$ in Chlorobenzene (CB). Finally, a layer of LiF was thermally

193   evaporated at a pressure of $1x10^{-6}$ torr if required. To fabricate the inverted PSCs, Indium Tin

194   Oxide (ITO) coated glass substrate was used. The rest of the fabrication procedure was the same

195   as mentioned above and at the top silver (Ag) electrode was deposited at a pressure of $1x10^{-6}$

196   torr. The active area of the devices was $1cm^2$.

197

198   **2.3. Absorption Measurements and Device Characterization**

199   After fabrication, all samples were transferred to a UHV environmental chamber with controlled

200   temperature and environment and optical feedthroughs. Depending on the test run, the samples

201   were exposed to either a $N_2$ atmosphere (99.9%) or dry air (80% $N_2$, 20% $O_2$) and relative

202   humidity was adjusted by injecting water vapor via a feed through and controlled in-situ with a

203   calibrated sensor (lower limit is 5%) used to maintain the relative humidity. Samples were placed

204   onto a heated stage with sample temperature measured using a thermocouple. In all experimental

205   runs two samples were tested under sulphur plasma class AAA lamp (Plasma-I systems GmbH)

206   at AM 1.5. For absorption studies, transmission mode measurements were conducted by using an

207   optical fiber of 400 µm core integrated with ocean optics spectrometer model HR4000. For

208   device studies, BNC feed through allowed the samples to be connected to an external Keithley

209   SMU. In this work, the time taken to reach 80% (T80%) of the original value  (absorption of

210   perovskite absorber layer ) or 50% of the final value (T50%) were calculated and were used as

211   the 'output responses' for each test run. To aid the analysis, a software package (Reliasoft) was

212   used for multivariate analysis. XRD measurements were performed using a Philips X-PERT

213   3040/60 instrument at 40kV voltage and 30mA current with CuKα radiation. SEM measurements

214   have been performed using Hitachi TM3000-table top SEM.

## 3. Results and Discussion

To analyze how changing the factors affect stability, the time taken for the samples to reach two particular lifetime points has been measured; T80% (defined as the time to reach 80% of the initial value) and T50% (for 50% of initial value). A life test model was developed that uses a least square polynomial model to express the effects in terms of the stress factors or environmental conditions. Least square mean values were calculated by assuming this model of the characteristic life time as shown in eq. 1.

$$y_i = f_0 + \sum_{k=1}^{z} f_k x_{nk} + \varepsilon_n \tag{1}$$

Where $y_i$ represents the response, $f_0$ is a constant fitted parameter, $f_1$ to $f_k$ are the fitting parameters for the individual coefficients, $x_{nk}$ represents the $n^{th}$ level of the $k^{th}$ predictor variable and $\varepsilon_n$ represents the standard variance error. Multiple '$y$' observations (representing the T80% or T50% time) can be expressed with the matrix in eq. 2.

$$y = \begin{bmatrix} y_1 \\ y_2 \\ \vdots \\ y_n \end{bmatrix} X = \begin{bmatrix} 1 & x_{11} & x_{12} & \cdot & x_{1n} \\ 1 & x_{21} & x_{22} & \cdot & x_{2n} \\ \vdots & \vdots & & \cdot & \cdot \\ 1 & x_{n1} & x_{n2} & \cdot & x_{nn} \end{bmatrix} \tag{2}$$

The matrix X is denoted as design matrix containing information about the level of the predictor variable. The main effect of the experimental factors can be solved using eq. 3 (Esbensen et al., 2018)

$$E_X = 2[\sum(y+) - \sum(y-)]/N \tag{3}$$

where $y+$ represents the high-level term, $y-$ represents the low-level terms and $N$ represents the total number of experiments. The main effects are assumed to have the same variance, defined as $\sigma^2$, given in eq. 4. Here $E_X$ represents the factors and $\mu$ is the calculated mean.

$$\sigma^2 = \frac{\sum(E_X - \mu)^2}{N-1} \tag{4}$$

In order to identify a regression line, the standard error must be accounted. The standard error of the estimate is a measure of the accuracy of predictions and given in eq. 5.

9

$$238 \qquad \sigma_{est} = \sqrt{\frac{\sum(Y_{real} - Y_{est})^2}{N}} \qquad (5)$$

239  Where $\sigma_{est}$ is the standard error of the estimate, $Y_{real}$ is an actual value and $Y_{est}$ is an estimated

240  value. The numerator is the sum of squared differences between the actual scores and the

241  predicted scores. The mean squared error is $F_{MS}$ dependent on the mean squared factor, which is

242  related to the variance of single quantity as shown in eq. 6.

243

$$244 \qquad F_{ms} = \frac{(E_X)^2}{N} \qquad (6)$$

245  Fitted mean values are obtained from the multivariate analysis for 'H' and 'L' values of

246  each factor. Figure 2 illustrates the variation of the fitted means for 'L' and 'H' levels of each

247  factor (predictors) calculated from multivariate analysis. To calculate the fitted means, least

248  square regression analysis has been applied to calculate the mean response values within a

249  factorial design (2-fold PB design in our case). Fitted means can be used to identify the variation

250  in the responses (T80% and T50% in this case) due to the change in the level of a particular

251  factor (i.e. 'L' to 'H' and vice versa). A systematic procedure to obtain Fig. 2 is given in *SI*

252  *(section S2)*. A higher value of fitted means for a particular level/factor is desirable as this will

253  lead to a higher T80% or T50% time. However, the difference between the fitted means of the

254  'L' and 'H' level in a particular factor shows how influential this factor is in affecting the overall

255  stability; a larger difference shows this factor has a greater impact on stability. The multivariate

256  analysis has enabled us to determine the significance of all the stress factors. The difference

257  between the larger and smaller value of fitted mean (FM) was calculated and plotted as a

258  function of stress factor in the order of significance in Fig. 3(a) for T80% and 3(b) for T50%.

259  From the data in Fig. 2, it is clear that for T80% and T50% responses, the presence of $O_2$ has the

260  most significant impact on the stability of the PSC, which is evidenced by the greatest difference

261  between the fitted means of the 'L' and 'H' level. The exposure of the absorber layer to $O_2$ and

262  light leads to the formation of superoxide ($O_2^-$) species, which react with the organic cation

263  ($CH_3NH_3^+$) of the photoexcited absorber layer. This mechanism is one of the root causes of

264  degradation in the presence of $O_2$ (Boyd et al., 2019 ; Bryant et al., 2016).

$$265 \qquad 4CH_3NH_3PbI_3 + O_2^- \rightarrow 4PbI_2 + 2I_2 + 2H_2O + 4CH_3NH_2 \qquad (7)$$
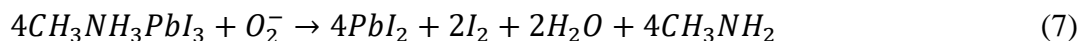
266         It has also been observed that the oxygen can diffuse into the solar cell structure and can

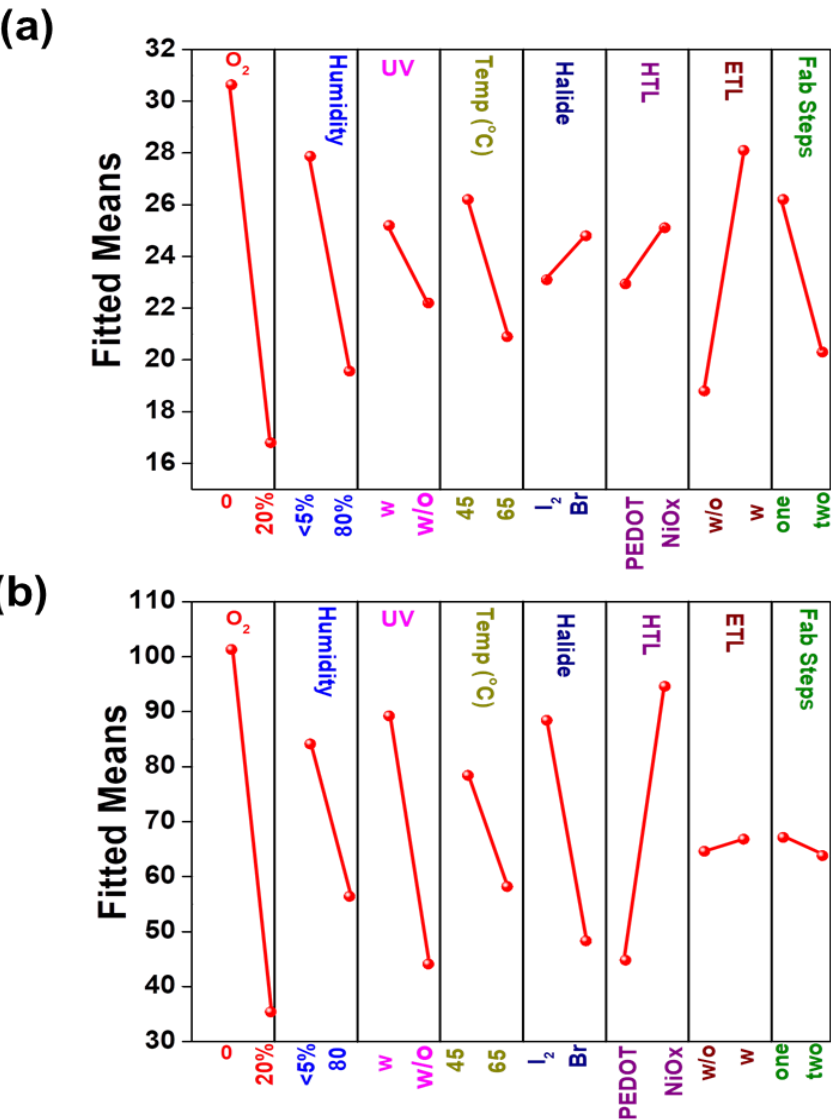267   become a more severe factor in the device instability.

268



**Fig. 2: Term effect plots of two-level Placket-Burman design completed using perovskite absorber layers. The results show perovskite's susceptibility to all explored main factors up to (a) T80% and (b) T50%.**

269   The next (second) most significant factor affecting the stability depends on whether one is

270   studying the degradation to T80% or T50%. In the case of T80%, the second most significant

271  factor was found to be the ETL. In this study, an inverted structure has been used, where the ETL

272  is the topmost layer. The ETL can restrict the ingress of $O_2$ and moisture depending upon its

273  morphology (Lin et al., 2018). However, PCBM is a hydrophobic layer its alone use cannot

274  restrict the ingress of $O_2$ and moisture through the PSC structure. It can act as a barrier for these

275  extrinsic factors by reducing gas permeation through it by the *n*-type doping (Wang et al., 2017).

276  As it is the topmost layer, it is likely to be affected by degradation first, then after the 'barrier'

277  layer is degraded; it has a lesser and lesser impact as time progresses (which is why it does not

278  feature so prominently in the T50% data in Fig. 3).

279  The third most important factor to impact upon T80% degradation time was found to be

280  the presence of humidity. It is known that perovskite absorber layer reacts with water and forms

281  $CH_3NH_3PbI_3$-$H_2O$ compound, which then dissociates into $CH_3NH_3I$ and (Song et al., 2016a;

282  Schlipf et al., 2019). This consequently leads to the degradation of perovskite absorber layer.

283  The next most significant factor appeared to be whether a two-step process was adopted

284  for absorber fabrication over a one-step process. This can be explained by considering the two-

285  step process of perovskite formation, which relies on the inter-diffusion of MAI into $PbI_2$.

286  However, this process is reported as a reproducible procedure, still this leaves the possibility of

287  unreacted $PbI_2$ in the perovskite, which was found to be the case in the present study by XRD

288  measurements (see *SI Fig. S5*).

289  The difference in fitted means becomes smaller for the remaining factors, so it becomes

290  more challenging to 'rank' relative severity of subsequent factors. However, it can be deduced

291  that reducing the temperature and filtering the UV light can improve the stability. This is to be

292  expected, as at elevated temperatures, $MAPbI_3$ dissociates into $PbI_2$, which is the main cause of

293  degradation. In addition, UV radiation leads to the excitation of electrons in the absorber layer.

294  These photo-excited electrons react with $O_2$ to form $O_2^-$ and leads to the degradation of

295  perovskite absorber layer. Finally, the data shows that to achieve higher stability, replacing

296  iodide ions with bromide ions in the absorber layer and by adopting $NiO_x$ as the HTL leads to

297  greater stability, when considering the time taken to reach T80%.

298  In case of T50%, the general trend for enhancing the stability has changed as compared to

299  T80% degradation. Now the order of significance of the factors affecting stability is $O_2$, HTL,

300  UV, halide type. $O_2$ is still the most significant factor that affects degradation to T50%.
301  However, the selection of HTL and the filtering of UV light are now the second and third most
302  significant factors. The impact of HTL on T50% is significantly larger in comparison to that on
303  T80%.

304      This is because the HTL can only interact with $O_2$ and moisture after their diffusion
305  through the PSC structure (ETL, thick absorber layer). The HTL contributes less in initial
306  degradation as a thick absorber layer protects it against these extrinsic factors (Boyd et al., 2019).
307  However, the lateral diffusion of these species also takes place and does still have a minor role in
308  the initial degradation of HTL. Among the HTLs used in this study, PEDOT: PSS has a high
309  absorptivity of moisture, as it is water-soluble. However, under continuous illumination, its
310  reactivity with moisture decreases due to the increase in temperature. Furthermore, PEDOT: PSS
311  degrades itself with time and undergoes a phase separation (PEDOT rich and PSS rich phases),
312  consequently the PEDOT rich phase becomes more susceptible towards $O_2$-induced degradation
313  (Norman et al., 2010). This might be contributing in still making $O_2$ a prominent factor in T50%
314  degradation. The next significant factors in the order of decreasing significance were halide
315  variation, humidity and temperature. Perovskite absorber layer in itself undergoes several
316  changes under continuous illumination including halide segregation, ion migration, and the
317  compositional degradation. These chemical changes become rapid in the presence of other
318  external factors like $O_2$ and moisture (Boyd et al., 2019; Song et al., 2016b) and become more
319  severe with prolonged exposure. This indicates that the composition of perovskite absorber layer
320  plays a more significant role in further 30% degradation than the initial degradation.

321      It has been observed from Fig. 3 that the order of significance of factors affecting the
322  degradation to T80% and to T50% was different. It has been explained in the previous section
323  how some factors such as $O_2$, the morphology of ETL and humidity can affect the initial
324  degradation and at a later stage, the decomposition of the absorber layer and internal degradation
325  of HTL can dominate the process. In the case of PSCs, there are some reports where different
326  states of degradation have been observed; initial fast degradation ('burn-in') and later slow or an
327  almost linear regime of degradation (Domanski et al., 2018; Domanski et al., 2017; Abate et al.,
328  2015). The degradation states were found dependent on different factors (intrinsic and extrinsic).
329  However, it has been observed that prolonged exposure of PSCs can cause severe degradation

330    mainly due to the degradation of organic materials, perovskite absorber layer/transport layer
331    interfaces and contact degradation.

332    Similar observations have been made in silicon PVs, where the dominant failure modes in
333    PV changes depending on the time it has been outdoors (or more specifically the current state of
334    degradation) i.e. solder contacts tend to fail early in the life cycle, ethylene-vinyl acetate (EVA)
335    discolouring occurs later. The discolouring is due to the bleaching oxygen and is a consequence
336    of prolonged exposure of EVA to UV radiation and temperature. This can also occur due to the
337    poor crosslinking and additives in the EVA formulation (Kuitche et al., 2014). We think this
338    work shows that PSCs have similar characteristics because we see that different factors have
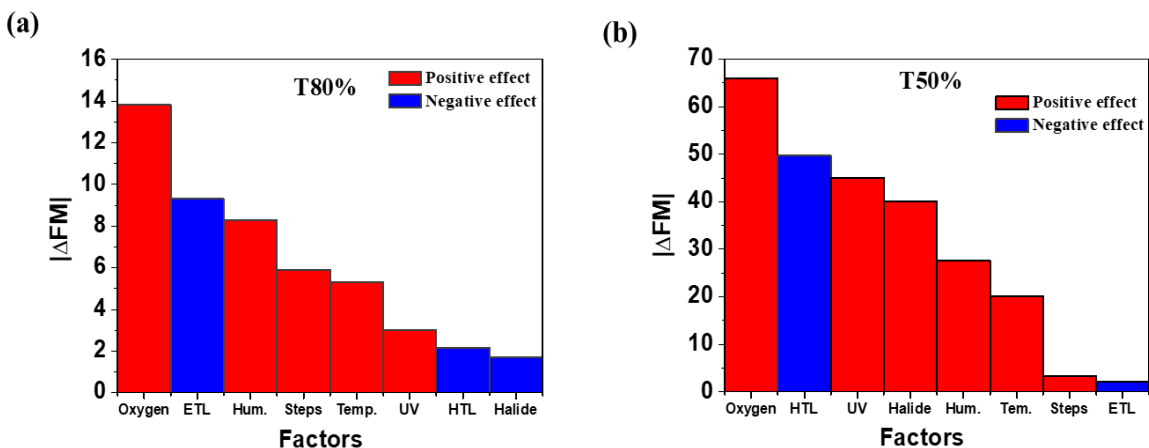339    greater or lesser affect depending on if the time is T80% or T50%.

340



**Fig. 3: The absolute difference between the highest and lowest fitted means (|ΔFM|) showing the significance of factors for (a) T80% and (b) T50% values. A positive effect indicates that the 'L' level is preferred for higher stability.**

341    To verify the studies, the most and least stable combinations were identified from PB screening
342    and compared for stability. The most stable structure was $NiO_x/MAPbBr_2I/PC_{70}BM/LiF/Ag$
343    (Device 'A') and the least was $PEDOT:PSS/MAPbI_3/PC_{70}BM/Ag$ (Device 'B'). PSCs with these
344    structures were fabricated. The PCE for Device 'A' was 5.0% and for Device 'B' was 8.2% with
345    an active area of $1cm^2$. The efficiency for Device 'A' is comparable to that reported with
346    MAPbBr_2I as an absorber layer (Zhao et al., 2014). The variation of photovoltaic parameters for
347    these devices has been shown in *SI (Fig. S4)* averaged from 5 devices. The variation of PCE as a

348    function of time is shown in Fig. 4(a) (in accordance with ISOS-D-1) and light soaking Fig. 4(b)

349    (in accordance with ISOS-L-2). Device 'A' shows a T80% of 255 hours during ISOS-D-1 testing

350    and 32 hours during ISOS-L-2 testing, whereas Device 'B' shows T80% of 35 hours and 3 hours

351    for the same respective tests. It is clear from both sets of experiments that Device 'A' shows

352    greater stability, confirming that this multivariate analysis approach can be used to identify the

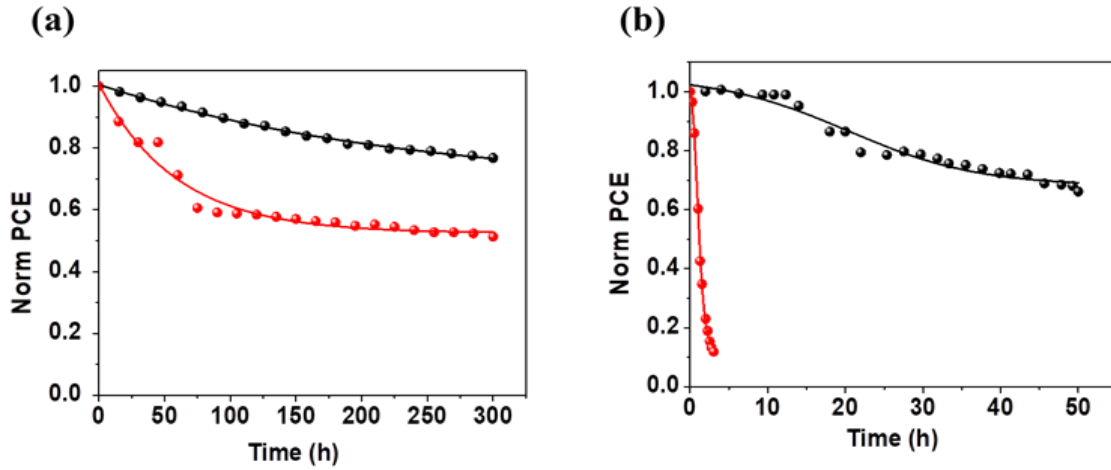353    best combination of materials to enhance device stability.



**Fig. 4: Normalized power conversion efficiency as a function of time for Device 'A' (black symbol and line) and Device 'B' (red symbol and line) solar cell measured by (a) ISOS D-1 (stored in the dark and ambient temperature) (b) ISOS-L2 (under continuous light exposure with controlled 65ºC temperature).**

354    Additional material analysis was conducted in order to investigate the degradation mechanisms.

355    XRD and SEM measurements can be effectively used to analyze the samples upon degradation

356    and identify the mechanism of this degradation. Here, SEM and XRD measurements were

357    performed on the fresh and degraded films for all test runs. First, the analysis for fresh samples

358    was performed to investigate the effect of device structure. One-step with anti-solvent treatment

359    processed films showed no pin-holes while the two-step processed film showed small size pin-

360    holes with low density (*SI Fig. S5*). MAPbI$_3$ fabricated by two-step process showed an unreacted

361    PbI$_2$ peak in the XRD measurements. Further, the NiO$_x$ supported better formation of perovskite

362    film in comparison to PEDOT:PSS, which was observed by SEM and XRD measurements (*SI*

363    *Fig. S6*). The effect of perovskite layer thickness was found more prominent on MAPbBr$_2$I films

364    (*SI Fig. S7*).

The PB approach can also be used to deduce some of these effects of degrading the samples by material analysis studies. This is somewhat difficult to do as the approach is primarily for studying multivariable using minimal test runs to acquire data quickly and not for detailed material studies. However, some trends can be observed to aid the understanding of degradation pathways.

Figure 5 shows the SEM images of fresh and degraded samples from Run 1 (as defined in Table 1). The fresh sample (Fig. 5(a)) did not show any film deformation or pinholes. The degradation of the film under continuous light illumination without any additional stress factors is shown in Fig. 5(b), where pin-holes of about 1um size can be observed in the samples. Fig. 5(c) shows the film degraded under continuous light illumination with humidity and $O_2$ (sample from run 11) and 5(d) with UV exposure (sample from run 12). The presence of UV light has caused the formation of small size pinholes with a larger density, but the humidity and $O_2$ affects the films more drastically leading to very large size deformities.

The results are consistent with other reports; the exposure to humidity and $O_2$ leads to decomposition of perovskite into its constituent materials (Song et al., 2016b). $MAPbI_3$ decomposes into MAI and $PbI_2$, which can further decompose into Pb and iodine (Juarez-Perez et al., 2018). This would account for the large sized pinholes observed in SEM images. The effect of light and UV can be explained by the reaction of photo excited electrons in perovskite with $O_2$ which form $O_2^-$. This $O_2^-$ reacts with the organic part of the perovskite layer, which leads to decomposition of perovskite absorber layer. However, the results highlight the relative severity and show how the presence of two or more stress factors can significantly accelerate the process of degradation of perovskite absorber layer. Although the optical and morphological analysis cannot guarantee a certain pattern in device degradation but it can assure valid stable operational conditions.
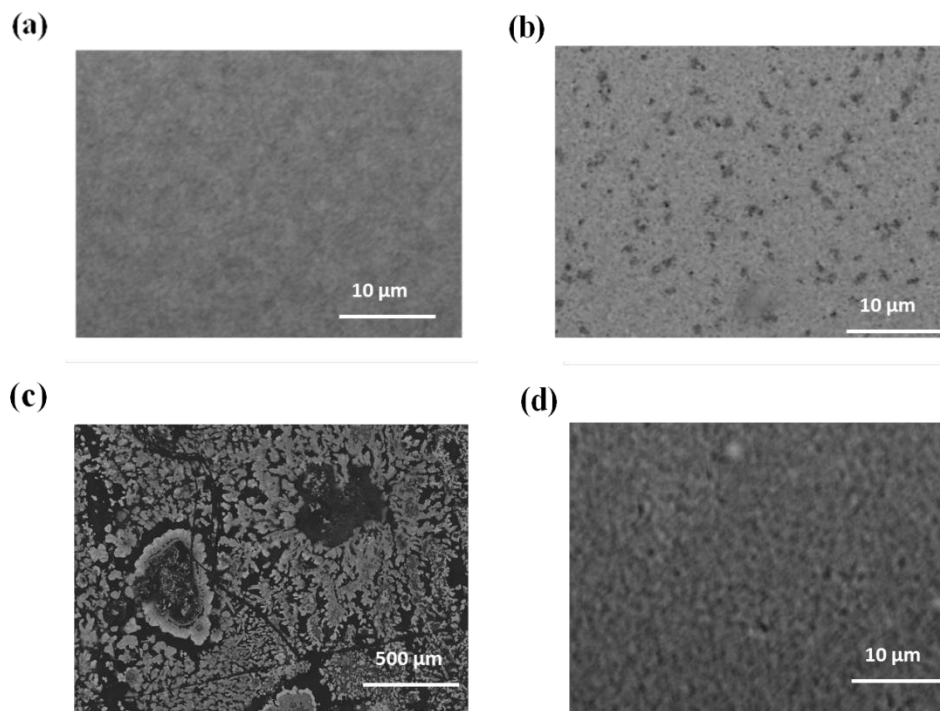
**Fig. 5: SEM image of (a) fresh sample (run 1), (b) sample degraded under continuous light exposure without any extrinsic stress (sample from run 1) and (c) with humidity and $O_2$ (sample from run 11) (d) with UV (sample from run 12).**

389    XRD measurements were used to study the differences in degradation between $MAPbBr_2I$ and

390    $MAPbI_3$ samples tested during the PB screening tests. Figure 6 shows the XRD spectra of fresh

391    and degraded (a) $MAPbBr_2I$ and (b) $MAPbI_3$ samples. In case of $MAPbBr_2I$, peaks

392    corresponding to several crystalline structures were observed in the fresh sample and are

393    highlighted in the Fig 6(a). All the crystalline peaks shifted to higher angles in the degraded

394    samples. This may be attributed to the slight decrease in d-spacing or phase change in perovskite

395    due to degradation. On the other hand, the effect of degradation on $MAPbI_3$ is different. There is

396    no major shift in the crystalline peaks; however, an additional peak of $PbI_2$ appeared (Fig. 6(b)).
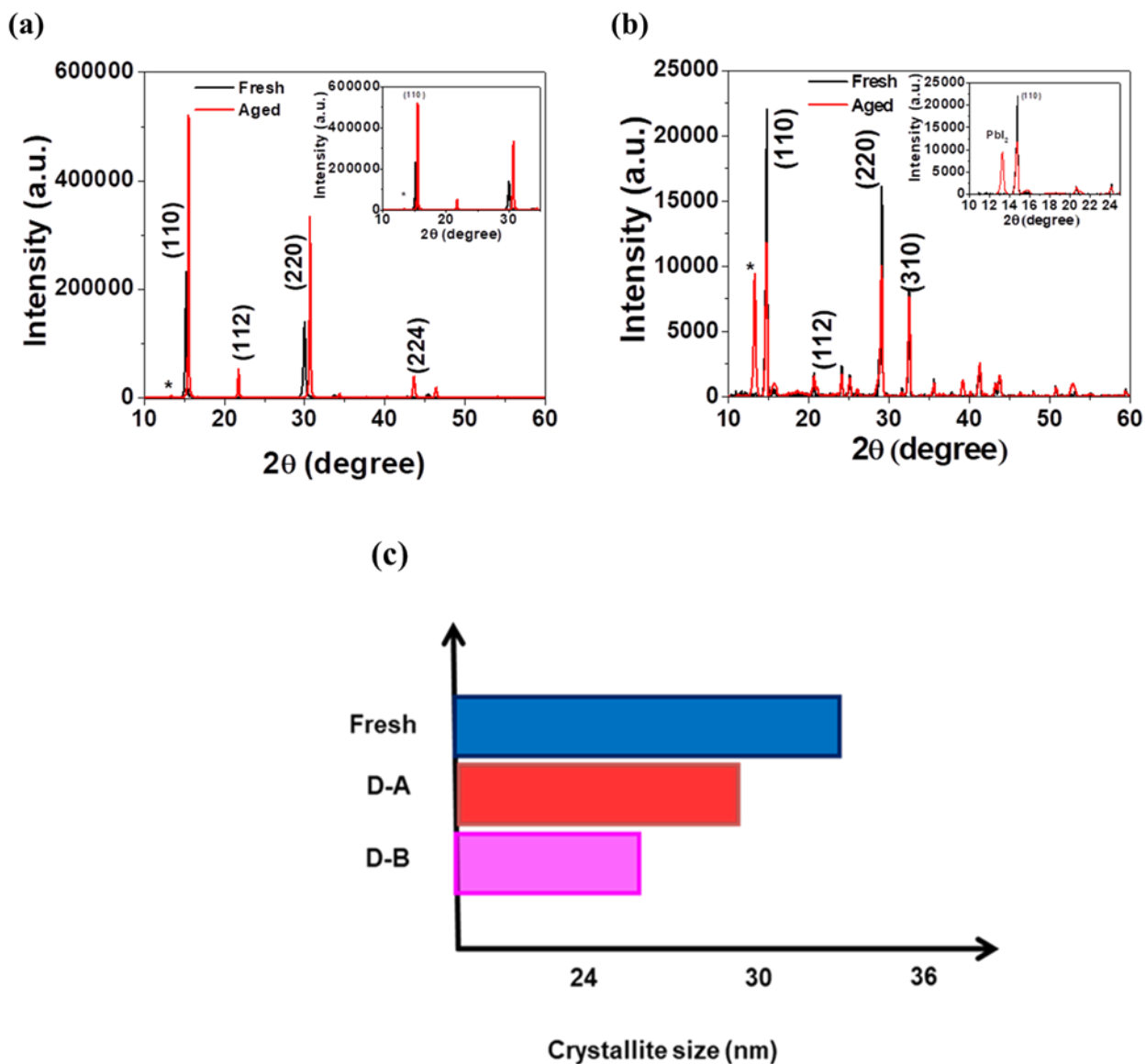
397

398

**Fig. 6: XRD spectrum of fresh and degraded (under humidity and O₂) (a) MAPbBr₂I, sample from run 2 (b) MAPbI₃, sample from run 11. Significant XRD peaks are marked in the figure (c) Crystallite size calculated from the XRD spectrum for fresh and degraded sample MAPbI₃. D-A: degraded sample under humidity and O₂ and D-B: degraded sample under heat and UV.**

399    Degradation can be quantified by crystallite size variation. The crystallite size was found to be

400    60±3 nm in case of fresh MAPbBr₂I sample. We have observed a shift in (110) crystalline peak

401    of diffraction towards the higher angle. This may be attributed to loss of iodide or phase change

402    in perovskite due to degradation (Cui et al., 2016). Indeed, perovskite swelling of more than 50

403    times (in the thickness) by aqueous solutions have been observed by Song et al. (Song et al.,

2015). The variation of crystallite is shown in Fig. 6(c) for MAPbI$_3$. The crystallite size was found to be 34 nm in fresh MAPbI$_3$ sample reduces to 29 nm in case sample exposed to O$_2$ and humidity and 25nm in case sample exposed to UV and temperature. This reduction in crystallite size is attributed to the change in morphological changes in the perovskite films under different stresses. As we have discussed earlier, MAPbI$_3$ decomposes into MAI and PbI$_2$, which can also decompose into Pb and iodine under O$_2$ and humidity. The perovskite layer also suffers from photo oxidation and phase change under UV and temperature. We have calculated the crystallite size of PbI$_2$ formed under these stresses. The crystallite size of PbI$_2$ was found to be 31 nm under humidity and O$_2$ stress and 12 nm under UV and 65°C. This may be a result of the difference in the rate of decomposition of MAPbI$_3$ into PbI$_2$ under both the conditions.

These results support the PB screening conclusions where we have observed that the presence of O$_2$ and humidity has severe impact on PSC stability, within this testing range.

## 4. Conclusions

A two-fold multifactorial analysis based on Plackett -Burman screening technique has been used to screen the most and least significant factors in the degradation of PSCs. In total 9 factors have been studied under 12 test runs; four extrinsic (O$_2$, humidity, temperature and UV exposure) and five intrinsic (transport layers, halide type, absorber layer thickness and perovskite deposition process). To our knowledge, this is one of the most comprehensive stability studies undertaken on PSCs in terms of factors studied. The data obtained has been analyzed by multivariate analysis and the fitted means corresponding to the high and low values of each stress factor have been used to deduce the most and least significant factors. This analysis enables us to select the materials and device configuration   to get the most stable PSC structure. We have fabricated the most stable and least stable PSC devices based on the conclusion made by PB screening and tested their reliability under ISOS-D1 and ISOS-L2 protocols. The time related to T80% degradation of most stable device was measured to be 255 hours and 32 hours under ISOS-D1 and ISOS-L2 protocols. SEM and XRD measurements have been performed to find the compressive details about the morphological and structural change in perovskite layer while subjected to different stress factors for all 12 runs.

436 **Supporting Information**

437 Specification of experimental runs used and time dependent absorption measurements, Time

438 dependent absorption measurements and calculation of fitted means; absorption spectrum of

439 perovskite absorber layers, decay curve for 12 experimental runs, calculated T80% and T50%

440 values for each experimental run; Device performance; SEM and XRD measurements of freshly

441 prepared and aged samples.

442

443

444

445

446

447

448

449

450

451

452

453

## References

Abate, A., Paek, S., Giordano, F., Correa-Baena, J.-P., Saliba, M., Gao, P., Matsui, T., Ko, J., Zakeeruddin, S. M., Dahmen, K. H., Hagfeldt, A., Gratzel, M., Nazeeruddin, M. K., 2015. Silolothiophene-linked triphenylamines as stable hole transporting materials for high efficiency perovskite solar cells, Energy Environ. Sci. 8, 2946–295.

Alves, A. S., Santos, R. d., 2014. Response Surface Methodology 1.

Boyd, C. C., Cheacharoen, R., Leijtens, T., McGehee, M. D., 2019. Understanding degradation mechanisms and improving stability of perovskite photovoltaics. Chem. Rev. 119, 3418-3451.

Briefs, A. M. C. T. Experimental design and optimisation (4): Plackett–Burman designs., 2013. Anal. Methods 5, 1901.

Bryant, D., Aristidou,N., Pont,S., Sanchez-Molina,I., Chotchunangatchaval, T. , Wheeler, S. , Durrant, J. R. , Haque, S. A., 2016. Light and oxygen induced degradation limits the operational stability of methylammonium lead triiodide perovskite solar cells. Energy Environ. Sci. 9, 1655–1660.

Cao, J., Wu, B., Chen, R. Wu, Y., Hui, Y., Mao, B.-W., Efficient, hysteresis-free and stable perovskite solar cells with ZnO as electron transport layer; effect of surface passivation., 2018. Adv. Mater. 30, 1705596 (1-9).

Christians, J. A., Schulz, P., Tinkham, J. S., Schloemer, T. H., Harvey, S. P., Tremolet de Villers, B. j., Spellinger, A., Berry, J. J., Luther, J. M., 2018a. Tailored interfaces of unencapsulated perovskite solar cells for > 1,000 hour operational stability. Nat. Energy 3, 68-74.

Christians, J. A. , Habisreutinger, S. N. , Berry, J. J. , Luther, J. M., 2018b. Stability in perovskite photovoltaics: a paradigm for newfangled technologies. ACS Energy Lett. 3, 2136-2134.

Cui, D., Yang, Z., Ren, X., Liu, Y., Wei, Q., Fan, H., Zeng, J., Liu, S., 2016. Color-Tuned perovskite films prepared for efficient solar cell applications. J. Phycs. Chem. C 120, 42-47.

Domanski, K., Roose, B., Matsui, T., Saliba, M., Turren-Cruz, S.- H., Correa-Baena, J. -P., Carmona, C. R., Richardson, Foster, J. M., Angelis, F. D., Ball, J. M., Petrozza, A., Mine, N., Nazeeruddin, M. K., Tress, W., Gra¨tzel, M., Steiner, U., Hagfeldt, A., Abate, A., 2017. Migration of cations induces reversible performance losses over day/night cycling in perovskite solar cells. Energy Environ Sci. 10, 604-613.

Domanski, K. , Alharbi, E. A. , Hagfeldt, A. , Grätzel, M. , Tress, W., 2018. Systematic investigation of the impact of operation conditions on the degradation behavior of perovskite solar cells. Nat. Energy 3, 61-67.

486 Edri, E., Kirmayer, S., Cahen, D., Hodes, G., 2013. High open-circuit voltage solar cells based
487 on organic−inorganic lead bromide perovskite. J. Phys. Chem. Lett. 4, 897-902.

488 Esbensen, K. H.' Swarbrick, B.' Westad, F.' Whitcomb, P.' Anderson, M., 2018. Multivariate
489 data analysis: an introduction to multivariate analysis, process analytical technology and quality
490 by design. CAMO Software AS' 6th Edition.

491 Gomes, T. C., Kumar, D., Fugikawa-Santos, L., Alves, N., Kettle, J., 2019. Optimization of the
492 anodization processing for aluminum oxide gate dielectric in ZnO thin film transistors by
493 multivariate analysis. ACS Comb. Sci. 21, 370-379.

494 Islam, M. B., Yanagida, M., Shirai, Y., Nabetani, Y., Miyano, K., 2019. Highly stable semi-
495 transparent MAPbI$_3$ perovskite solar cells with operational output for 4000h. Sol. Energy Mater.
496 and Sol. Cells 195, 323-329.

497 Jain, S. P., Singh, P. P., Javeer, S., Amin, P. D. Use of Placket–Burman statistical design to study
498 effect of formulation variables on the release of drug from hot melt sustained release extrudates.,
499 2010. AAPS Pharm. Sci. Tech. 11, 936–944.

500 Juarez-Perez, E. J., Ono, L. K., Maeda, M., Jiang,Y., Hawasha, Z., Qi, Y., 2018.
501 Photodecomposition and thermal decomposition in methylammonium halide lead perovskites
502 and inferred design principles to increase photovoltaic device stability. J. Mater. Chem. A  6,
503 9604-9612.

504 Kanda, H., Shibayama, N., Uzum, A., Umeyama, T., Imahori, H., Ibi, K., Seigo, I., 2018. Effect
505 of Silicon Surface for Perovskite/Silicon Tandem Solar Cells: Flat or Textured. *ACS* Appl.
506 Mater. Interfaces 10, 36016-35024.

507 Kim, J. H., Liang, P. W., Williams, S. T., Cho, N., Chueh, C.C., Glaz,  M. S.,  Ginger, D. S., Jen,
508 A. K.Y., 2015. High-Performance and environmentally stable planar heterojunction perovskite
509 solar cells based on a solution-processed copper-doped nickel oxide hole-transporting layer.
510 Adv. Mater. 27, 695-701.

511 Koehl, M., Heck, M., Wiesmeier, S., Wirth, J., 2011. Modeling of the nominal operating cell
512 temperature based on outdoor weathering. Solar Energy Materials & Solar Cells 95, 1638-1646.

513 Kong, W., Rahimi-Iman, A., Bi, G., Dai, X., Wu, H., 2016. Oxygen Intercalation Induced by
514 Photocatalysis on the Surface of Hybrid Lead Halide Perovskites. J. Phys. Chem. C 120, 7606–
515 7611.

516 Kuitche, J. M., Pan, R., Tamizhmani, G., 2014. Investigation of dominant failure mode(s) for
517 field-aged crystalline silicon pv modules under desert climatic conditions. IEE J.  Photov. 4, 814-
518 826.

519  Li, X., Bi, D., Yi, C., Décoppet, J. D., Luo, J., Zakeeruddin, S. M., Hagfeldt, A., Grätzel, M.,
520  2016. A vacuum flash–assisted solution process for high-efficiency large-area perovskite solar
521  cells. Science 353, 58-62.

522  Lin, C.-T., Pont, S., Kim, J., Du, T., Xu, S., Li, X., Bryant, D., Mclachlan, M. A., Durrant, J. R.,
523  2018. Passivation against oxygen and light induced degradation by the PCBM electron transport
524  layer in planar perovskite solar cells. Sustainable Energy Fuels 2, 1686-1692.

525  Liu, D., Gangishetty, M. K., Kelly, T. L., 2014. Effect of $CH_3NH_3PbI_3$ thickness on device
526  efficiency in planar heterojunction perovskite solar cells. J. Mater. Chem. A 2, 19873-19881.

527  Lopez, C. A., Martinez-Huerta, M. V., Alvarez-Galvan, M. C., Kayser, P., Gant, P., Castellanos-
528  Gomez, A., Fernandez-Diaz, M. T., Fauth, F., Alonso, J. A., 2017. Elucidating the
529  methylammonium (MA) conformation in $MAPbBr_3$ perovskite with application in solar cells.
530  Inorg. Chem. 56, 14214-14219.

531  Misra, R. K. , Aharon, S. , Li, B. , Mogilyansky, D. , Visoly-Fisher, I. , Etgar, L. , Katz, E. A.,
532  2015. Temperature and component-dependent degradation of perovskite photovoltaic materials
533  under concentrated sunlight. J. Phys. Chem. Lett. 6, 326-330.

534  Norman, K., Madsen, M. V., Gevorgyan, S. A., Krebs, F. C., 2010. Degradation patterns in water
535  and oxygen of an inverted polymer solar cell. J. Am. Chem. Soc. 132, 16883-16892.

536  Saliba, M., Matsui, T., Seo, J. Y., Domanski, K., Correa-Baena, J. P., Nazeeruddin, M. K.,
537  Zakeeruddin, S. M., Tress, W., Abate, A., Hagfeldt, A., Grätzel, M., 2016. Cesium-containing
538  triple cation perovskite solar cells: improved stability, reproducibility and high efficiency.
539  Energy Environ. Sci. 9, 1989-1997.

540  Sahli, F., Werner, J., Kamino, B. A., Brauninger, M., Monnard, R., Salomon, B. P., Barraud, L.,
541  Ding, L., Leon, J. J. D., Sacchetto. D., Canttaneo, G., Despeisse, M., Boccard, M., Nicolay, S.,
542  Jeangros, Q., Niesen, B., Ballif, C., 2018. Fully textured monolithic perovskite/silicon tandem
543  solar cells with 25.2% power conversion efficiency. Nat. Mater. 17, 820-826.

544  Schlipf, J., Hu, Y., Pratap, S., Biebmann, L., Hohn, N., Porcar, L., Bein, T., Docampo, P.,
545  Muller-Buschbaum, P., 2019. Shedding light on the moisture stability of 3d/2d hybrid perovskite
546  heterojunction thin films. ACS Appl. Energy Mater. 2, 1011-1018.

547  Song, Y., Lyi, N., Hoshide, T., Ozawa, T. C., Ebina, Y., Ma, R., Miyamoto, N., Sasaki, T., 2015.
548  Accordion-like swelling of layered perovskite crystals via massive permeation of
549  aqueoussolutions into 2D oxide galleries. Chem. Commun. 51, 17068-17071.

550  Song, Z., Abate, A., Watthage, S. C., Liyanage, G. K., Phillips ,A. B., Steiner, U., Graetzel, M.,
551  Heben, M. J., 2016a. Perovskite solar cell stability in humid air: partially reversible phase
552  transitions in the $PBI_2$-$CH_3NH_3I$-$H_2O$ system. Adv. Energy Mater. 6, 1600846.

553 Song Z., Abate ,A., Watthage, S.C., Liyanage, G.K., Phillips, A.B., Steiner, U., Graetzel, M.,
554 Heben, M. J., 2016b. In-situ observation of moisture-induced degradation of perovskite solar
555 cells using laser-beam induced current. Photovoltaic Specialists Conference (PVSC), 1202-1206.

556 Strabks, S. D., Eperon, G. E., Grancini, G., Menelaou, C., Alcocer, M. J. P. , Leijtens, T., Herz,
557 L. M., Petrozza, A., Snaith, H. J., 2013. Electron-hole diffusion lengths exceeding 1 micrometer
558 in an organometal trihalide perovskite absorber. Science 342, 341-344.

559 Turak, A., Zgierski, M. Z., Dharma-Wardana, M. W. C., 2017. LiF doping of $C_{60}$ studied with X-
560 ray photoemission Shake-Up Analysis. ECS J. Solid State Sci. Technol. 6, M3116-M3121.

561 Wang, Y., Dong, S., Miao, Y., Li, D., Qin, W., Cao, H., Yang, L., Li, L., Yin, S., 2017. BCP as
562 additive for solution-processed PCBM electron transport layer in efficient planar heterojunction
563 perovskite solar cells. IEEE J. Photov. 7, 550-557.

564 Waśko, A, Kordowska-Wiater, M., Podlesny, M., Polak-Berecka, M., Targonski, Z., Kubik-
565 Komar, A., 2010. The Plackett-Burman design in optimization of media components for biomass
566 production of *Lactobacillus rhamnosus* OXY. Acta Biol. Hung. 61, 344–355.

567 Xiao, Z.' Bi, C.' Shao, Y.' Dong, Q.' Wang, Q.' Yuan, Y.' Wang, C.' Gao, Y.' Huang, J., 2014.
568 Efficient, high yield perovskite photovoltaic devices grown by interdiffusion of solution-
569 processed precursor stacking layers. Energy Environ. Sci. 7, 2619-2623.

570 You, J.' Yang, Y.' Hong, Z.' Song, T.-B.' Meng, L.' Liu, Y.' Jiang, C.' Zhou, H.' Chang W.-H.'
571 Li, G.' Yang, Y., 2014. Moisture assisted perovskite film growth for high performance solar
572 cells. Appl. Phys. Lett. 105, 183902.

573 You, J.' Meng, L.' Song, T.-B., Guo, T.-F., Yang, Y(M.).' Chang, W.-H., Hong, Z.' Chen, H.'
574 Zhou, H.' Chen, Q.' Liu, Y.' Marco, N. D.' Yang, Y., 2016. Improved air stability of perovskite
575 solar cells via solution-processed metal oxide transport layers. Nat. Nanotech. 11, 75-81.

576 Zhao, Y., Nardes, A. M., Zhu, K., 2014.Mesoporous perovskite solar cells: Material
577 composition, charge-carrier dynamics, and device characteristics. Faraday, Discuss. 176, 301.

578 Zhou, Y., Yin, X., Luo, Q., Zhao, X., Zhou, D., Han, J., Hao, F., Tai, M., Li, J., Liu, P., Jiang,
579 K., Lin, H., 2018. Efficiently improving the stability of inverted perovskite solar cells by
580 employing polyethylenimine-modified carbon nanotubes as electrodes. ACS Appl. Mater.
581 Interfaces 10, 31384-31393.

582